Defect-induced Asymmetrical Mechanical Behavior in Shape Memory Zirconia:

A Phase-Field Investigation

Cheikh Cissé and Mohsen Asle Zaeem\*

Department of Mechanical Engineering, Colorado School of Mines, 1500 Illinois street, Golden, CO 80401, USA

\*Corresponding author; E-mail: <u>zaeem@mines.edu</u> (M. Asle Zaeem)

Abstract

An elastoplastic phase-field model is used to investigate the deformation mechanisms of yttria stabilized tetragonal zirconia in presence of defects. A remarkable tension-compression asymmetry is detected. A higher strength and a lower degree of transformation are observed in compression than in tension. Also, deformation mechanism is asymmetric depending on the crystal orientation. For some cases (other cases), phase transformation is absent in tension (in compression), while both transformation and plasticity are present in compression (in tension). Such tension-compression asymmetry is attributed to activation of different monoclinic variants with different Eigen strain tensors in tension versus compression. Results also reveal a higher degree of transformation and plasticity with lower onset stresses as the void size increases. Elliptic voids exhibit a directional effect with a maximum stress intensity factor of 5.6 MPa.m<sup>1/2</sup> when the long semi-axis is diagonally oriented with respect to the loading direction, and this prediction is comparable to experiments.

Keywords: Shape memory ceramics; zirconia; defects; phase-field modeling; plasticity.

### 1. Introduction

The ever-increasing complexity in engineering applications require high-performance materials [1]. A prime example is the need of strong, temperature-resistant, and damage tolerant materials for full-fledged development of next-generation hypersonic vehicles, fuel-efficient jet engines, and nuclear energy reactors [2-4]. Ceramics are usually strong and temperature/corrosion resistant making them potential candidates for such applications, but they suffer from low damage tolerance. Such multiple requirements cannot be currently satisfied simultaneously [5]. A core issue is that all materials are prone to cracks when their deformed microstructure reaches its strain-hardening limit [5]. Therefore, a main engineering challenge is to increase the fracture toughness which is a critical mechanical property determining the structural integrity and reliability of engineering components and devices.

It is well-established that plastic deformation and phase transformation have the commonality of increasing fracture toughness via strain energy absorption and stress relaxation in shape memory alloys (SMAs) [6-8]. However, in the case of shape memory ceramics, the brittleness is not easy to overcome. While some transformable ceramics such as yttria-stabilized tetragonal zirconia (YSTZ) can potentially increase fracture toughness, plastic deformation is mostly limited therein and the transformation-induced volume expansion may also result in microcracking [9, 10]. Fracture behavior of such materials need to be fully understood, especially at the lower length scales where ubiquitous nanoscale defects control the brittle fracture behavior.

YSTZ ceramics, with dopant concentration less than 4% mol., display a reversible tetragonal-to-monoclinic phase transformation (TMPT) and possible plastic yielding [11-13]. This TMPT is accompanied by a significant shape recovery of up to 7% shear strain, and a volume expansion of 3~5% [14], which induces shape memory effect, superelasticity [15], and transformation toughening [16]. Such a high capacity to accommodate the shape variation and large inelastic strain, along with their outstanding strength, hardness, and resistance to oxidation and corrosion have paved the way for unique engineering applications of YSTZ, including thermal barrier coating, wear and bearing parts [13], refractors, gas sensors, and pacifiers [17, 18]. However, their limited plasticity and relatively low damage tolerance, particularly their tensile brittleness [19], are the main obstacles to their extended applicability [5]. During material processing or service, the volume expansion associated with the TMPT can generate defects (nano and micro voids and cracks) at localized regions [20-22]. On the other hand, under some conditions, the same volume expansion can heal/close the some cracks

as they form [23, 24], which can limit and/or delaying crack growth and toughen the material during service [25]. Therefore, understanding how TMPT and plasticity interact with flaws is of particular importance in YSTZ where the crystal orientation is a determinant factor of the deformation mechanisms [26, 27] and mechanical properties [28].

Since the first fatigue study of zirconia by Dauskardt and Ritchie [29], researchers have found that all toughened ceramics display a degradation of their mechanical properties when subjected to cyclic loads [30-32]. The fracture in zirconia is reported to initiate at defects (voids, cracks and flaws) [33]. Likewise, interlamellar gaps, open pores and microcracks were evidenced on the fracture surface of zirconia [34] (see Figure 1a). Microscopic observations also highlight failure initiation sites in 3Y-STZ dominated by pores and voids [22] (see Figure 1 b). These results were confirmed by the scanning electron microscopy (SEM) observations of Govila [35] and Casellas et al. [36] showing that pores constitute important failure origins in YSTZ. Experimental fatigue studies in YSTZ [21, 31, 37], magnesia-partially stabilized zirconia [38] and ceria-stabilized tetragonal zirconia [20, 39] reveal that TMPT-induced cracktip shielding ensures a stable/small crack growth under constant load, which progressively contribute to deterioration of strength during cyclic loading [40].

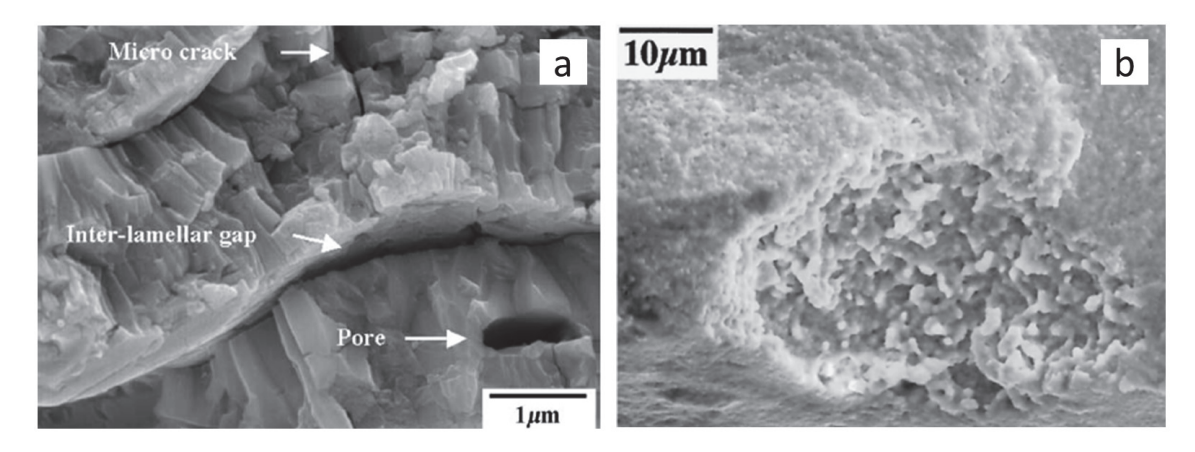


Figure 1. (a) Cross-sectional SEM micrograph showing the defect morphology of as-sprayed zirconia coats [34], and (b) Failure-initiation sites at pores[22].

Quantitative understanding of the deformation mechanisms of defect filled zirconia ceramics is needed [41]. Because experimental methods are limited by their time and length scales, numerical approaches such as molecular dynamics (MD) and phase-field modelling (PFM) stand out as practical alternatives [42]. At the atomistic level, Zhang and Asle Zaeem conducted MD simulations of YSTZ to determine the critical crack width ensuring its closure

[43], self-healing, dislocation migration and formation of amorphous phase in single crystals [25], nanoscale flaw tolerance in bicrystal [9], and competition between twin-boundary-induced and void-induced TMPT in polycrystals [44]. At the microscale, Mamivand et al. developed an elastic PFM [45] to study transformation toughening ahead of a crack tip in zirconia under monotonic tensile loading [46]. In a recent work, Cissé and Asle Zaeem [27] proposed a fully thermomechanical coupled elastoplastic PFM to investigate the orientation-dependent deformation mechanisms in 3Y-STZ (TMPT and plasticity). This robust and transferable model was also used later to study the elastocaloric effect in SMAs [47, 48], predict the fracture toughening in SMAs [49]. This model has been recently extended to incorporate the asymmetry of both martensitic transformation and plasticity, thermomechanical training and stress-assisted two-way shape memory effects [50]. Nonetheless, these considerable efforts have not been able to fully explain the very low fatigue life of zirconia-based shape memory ceramics.

The objective of this work is to numerically unveil how TMPT and plasticity interact with defects and provide insights on the effects of the shape, orientation, size and distribution of defects on localized and generalized thermomechanical behaviors in compression and tension of specifically orientated 3Y-STZ single crystals. Even if dislocation-mediated plasticity is temperature-dependent both in tetragonal and monoclinic phases, our work is conducted at high temperature where dislocations are mobile, which help simplify the formulation. The simulations are aimed to provide the deformation mechanisms and potentially guide the future experiments for enhancing 3Y-STZ fracture toughness. The rest of this article paper is organized in three sections; Section 2 gives the PFM and governing equations, Section 3 is dedicated to the simulation results, and Section 4 provides conclusive perspectives.

#### 2. Thermo-Elastic-Plastic Phase-Field Model

PFM is a powerful computational method that enables access to nano and micro length and time scales to investigate the evolution of nano/microstructures during phase transformation [51]. It uses orders parameters (OPs) as state variables to describe the involved processes. The TMPT can be well described by PFM using non-conserved long-range OPs, noted by  $\eta_v(\mathbf{r},t)$  for the  $v^{th}$  monoclinic variant (product phase) [45]. A full forward transformation into the  $v^{th}$  variant corresponds to  $\eta_v = 1$ , whereas  $\eta_v(\mathbf{r},t) = 0$  expresses an absence of the  $v^{th}$  variant. The total free energy  $F_{tot}$  of the system is composed of the chemical or bulk free energy

 $(F_{bk})$ , the gradient free energy  $(F_{gd})$ , the thermal free energy  $(F_{th})$ , and the elastic free energy  $(F_{el})$ .

### 2.1 Chemical free energy

The chemical free energy is the non-equilibrium homogeneous free energy driving the TMPT under stress-free conditions. Its density is defined as a 2-4-6 Landau polynomial of the primary OPs [51] so that to be insensitive to their signs and their permutations:

$$F_{ch}(\eta_p, T) = \frac{A(T)}{2} \sum_{v=1}^{N} \eta_v^2 - \frac{B(T)}{4} \sum_{v=1}^{N} \eta_v^4 + \frac{C(T)}{6} \left(\sum_{v=1}^{N} \eta_v^2\right)^3, \tag{1}$$

where N is the total number of monoclinic variants, and A(T), B(T) and C(T) are positive temperature-dependent coefficients that can be calibrated from the transition temperature, equilibrium OPs, and transformation latent heat [52]. They are related to the energy gap between tetragonal (equivalent to austenite phase) and monoclinic (equivalent to martensite phase),  $\Delta F(T)$ , as follows,

$$B(T) = 4A(T) - 12\Delta F$$
,  $C(T) = 3A(T) - 12\Delta F$ , and  $\Delta F(T) = Q(T/T_0 - 1)$ , (2)

where Q is the latent heat of phase transformation, and  $T_0$  is the equilibrium temperature. We proposed the following continuous function of temperature for coefficient A(T) [47, 50] so that simulate complete thermochemical deformation and account for the nonlinear increase of the critical transformation stress (CTS):

$$A(T) = \begin{cases} Q \exp\left[k_1\left(\frac{T}{T_0} - 1\right)\right], & \text{for } T \leq T_0 \\ Q \exp\left[k_2\left(\frac{T}{T_0} - 1\right)\right], & \text{for } T > T_0 \end{cases}$$
(3)

where  $k_1$  and  $k_2$  are positive constants.

#### 2.2 Gradient free energy

While the OPs are assumed to be homogeneous within each phase/domain, they change smoothly across the narrow regions called interfaces that separate the tetragonal and monoclinic phases. The gradient free energy is a heterogeneous penalty-like term for the spatial variations of the OPs. It helps guarantee the smooth phase transformation across the interfaces. An isotropic formulation of its density gives this simplified expression:

$$G_{gd}(\eta_1, \eta_2, ..., \eta_m) = \frac{1}{2}\beta \sum_{v=1}^{N} (\nabla \eta_v)^2,$$
 (4)

where  $\nabla$  is the gradient operator, and  $\beta$  is a coefficient related to the energy and/or thickness of the interface so that an appropriate value should replicate its energy density or finite width. For instance, Yeddu et al. [53] derived the following expression of the gradient energy coefficient:

$$\beta_0 = \frac{3\sqrt{2}}{4}\chi\xi,\tag{26}$$

where  $\chi$  is the interfacial energy, and  $\xi$  is the interface thickness.

# 2.3 Thermal free energy

The thermal free energy is a function of temperature and its density is given by the classic equation [50]

$$G_{th}(T) = C_p \left[ (T - T_0) - T ln \left( \frac{T}{T_0} \right) \right], \tag{5}$$

where  $C_p$  is the specific heat of the tetragonal and monoclinic phases.

### 2.4 Elastic free energy

The elastic free energy helps accommodate the microstructural changes due to the stretching/compression of atoms within the tetragonal phase and/or the lattice compatibility along the different interfaces during the TMPT. Its density is expressed as

$$F_{el}(\boldsymbol{\varepsilon}^{el}, \eta_v) = \frac{1}{2} \boldsymbol{\varepsilon}^{el} : \boldsymbol{K}(\eta_v) : \boldsymbol{\varepsilon}^{el} = \frac{1}{2} (\boldsymbol{\varepsilon} - \boldsymbol{\varepsilon}^{tr} - \boldsymbol{\varepsilon}^{pl}) : \boldsymbol{K}(\eta_v) : (\boldsymbol{\varepsilon} - \boldsymbol{\varepsilon}^{tr} - \boldsymbol{\varepsilon}^{pl}), \tag{6}$$

where  $K(\eta_v)$  is the equivalent stiffness tensor,  $\varepsilon(r)$  is the total strain tensor describing the macroscopic shape of the system,  $\varepsilon^{tr}(r)$  is the transformation strain tensor,  $\varepsilon^{pl}(r)$  is the plastic strain tensor, and  $\varepsilon^{el}(r)$  is the elastic strain tensor at a given location r. The elastic inhomogeneity is considered by defining an equivalent stiffness tensor  $K(\eta_v)$  given by [27, 50]:

$$K(\eta_v) = K^T + \left| \sum_{v=1}^m \eta_v \right| (K^M - K^T), \tag{7}$$

in which  $K^T$  and  $K^M$  refer to the stiffness tensor of the tetragonal and monoclinic phases, respectively. The transformation strain tensor  $\varepsilon^{tr}$  is related to the stress-free eigen strain tensor  $\varepsilon^{00}$  of the different monoclinic variants by [27, 50]:

$$\boldsymbol{\varepsilon}^{tr} = \sum_{\nu=1}^{N} \eta_{\nu}^{2} \boldsymbol{\varepsilon}_{\nu}^{00}. \tag{8}$$

Since we study crystals having different orientations, we will apply rotation operations to transfer the stress-free strain tensor and elastic stiffness matrix from the local coordinates of the different single crystals to the same global coordinate system, so that the short axis  $a_t$  and long axis  $c_t$  of the tetragonal phase coincide with the x and z-directions, respectively:

$$\varepsilon_{ij}^{G00} = \mathbf{R}_{ik} \mathbf{R}_{jl} \varepsilon_{kl}^{00} , \qquad (9)$$

$$C_{ijkl}^G = \mathbf{R}_{im} \mathbf{R}_{jn} \mathbf{R}_{ko} \mathbf{R}_{lp} C_{mnop}, \tag{10}$$

in which,  $\varepsilon_{kl}^{00}$  and  $C_{mnop}$  are the elements of the eigen strain tensor and elastic stiffness matrix in the local coordinate systems, respectively,  $\varepsilon_{ij}^{G00}$  and  $C_{ijkl}^{G}$  are their representations in the global coordinate system, and  $\mathbf{R}_{ij}$  is a rotation matrix which, for a crystal having an orientation angle  $\varphi$ , is given by

$$\mathbf{R}_{ij}(\varphi) = \begin{bmatrix} \cos(\varphi) & \sin(\varphi) \\ -\sin(\varphi) & \cos(\varphi) \end{bmatrix}. \tag{11}$$

A complete computation of the plastic strain requires a yield criterion, a hardening rule, and a plastic flow rule. We use a  $J_2$ -type yield criterion along with the loading-unloading condition

$$F_y = \hat{\sigma}_{vm}(\boldsymbol{\sigma}, \varphi) - \sigma_y = 0 \text{ and } \frac{\partial F_y}{\partial \boldsymbol{\sigma}} : \dot{\boldsymbol{\sigma}} > 0,$$
 (12)

in which  $\hat{\sigma}_{vm}$  is a modified von Mises equivalent stress accounting for the orientation dependency [27], and  $\sigma_y$  is the yield stress. These specific stress variables are expressed, respectively, as

$$\hat{\sigma}_{vm}(\boldsymbol{\sigma}, \varphi) = \cos^2(2\varphi) \cdot \sqrt{\sigma_{xx}^2 + \sigma_{zz}^2 - \sigma_{xx}\sigma_{zz} + 3\sigma_{xz}^2},$$

$$\sigma_y = \sigma_0 + H_y \varepsilon_{pq}^{\text{pl}},$$
(13)

where  $\sigma_{xx}$ ,  $\sigma_{zz}$ , and  $\sigma_{xz}$  are the two-dimensional (2D) components of the stress tensor,  $\sigma_0$  is the initial yield stress,  $H_y$  is the hardening modulus, and  $\varepsilon_{pq}^{\rm pl}$  is the equivalent plastic strain that reads

$$\varepsilon_{pq}^{\text{pl}} = \frac{2}{3} \sqrt{\varepsilon_{xx}^2 + \varepsilon_{zz}^2 - \varepsilon_{xx}\varepsilon_{zz} + 3\varepsilon_{xz}^2},$$
(14)

where  $\varepsilon_{xx}^{pl}$ ,  $\varepsilon_{zz}^{pl}$ , and  $\varepsilon_{xz}^{pl}$  are the components of the plastic strain tensor.

### 2.5. Governing equations

### 2.5.1 Evolution of transformation order parameters

The time and space evolutions of OPs are obtained by solving by time-dependent Ginzburg-Landau (TDGL) equation [54] relating their rates to the variational form of the total free energy with respect to the same OPs:

$$\frac{\partial \eta_{v}}{\partial t} = -M \frac{\partial F}{\partial \eta_{v}},\tag{15}$$

where M is the kinetic coefficient describing the mobility of the interfaces.

### 2.5.2 Evolution of temperature

The rate-dependency of TMPT is caused by the heat release/absorption during forward/reverse phase transformation, which changes the temperature in the material under adiabatic deformation. The time evolution and space distribution of the temperature is given by the heat conduction equation:

$$\rho C_p \frac{\partial T}{\partial t} = \lambda \nabla^2 T + \dot{q} \,, \tag{16}$$

where  $\dot{q}$  is the rate of heat source, and  $\lambda$  is the thermal conductivity of the material. Assuming that the rate of internal heat source is related to not only the latent heat of phase transformation, but also the intrinsic dissipation of plasticity, the rate of heat source becomes:

$$\dot{\mathbf{q}} = \langle \sigma_{vm} - \sigma_{y} \rangle \dot{\varepsilon}_{eq}^{pl} + \sum_{v=1}^{m} Q \dot{\eta}_{v}, \tag{17}$$

where  $\dot{\varepsilon}_{eq}^{pl}$  is a scalar denoting the rate of equivalent plastic strain, and  $\langle X \rangle$  denotes the positive part of scalar X.

### 2.5.3 Evolution of plastic strain

The evolution of the plastic strain is obtained from the normality rule and the consistency condition so that the plastic flow rule reads

$$\dot{\boldsymbol{\varepsilon}}^{pl} = \dot{\gamma} \frac{\partial F_{\gamma}}{\partial \boldsymbol{\sigma}},\tag{18}$$

where  $\dot{\gamma}$  is the rate of the plastic strain magnitude and is obtained from the consistency condition:

$$\dot{F}_{y} = \frac{\partial F_{y}}{\partial \boldsymbol{\sigma}} : \dot{\boldsymbol{\sigma}} + \frac{\partial F_{y}}{\partial \gamma} \dot{\gamma} = 0. \tag{19}$$

Discretizing the Hooke's law as

$$\dot{\boldsymbol{\sigma}} = \dot{\boldsymbol{C}}(\eta_v) : \boldsymbol{\varepsilon}^{el} + \boldsymbol{C}(\eta_v) : (\dot{\boldsymbol{\varepsilon}} - \dot{\boldsymbol{\varepsilon}}^{tr} - \dot{\boldsymbol{\varepsilon}}^{pl}), \tag{20}$$

the rate of the plastic multiplier can be written as

$$\dot{\gamma} = \frac{N^p : \left[C : (\dot{\varepsilon} - \dot{\varepsilon}^{tr}) + \dot{C} : \varepsilon^{el}\right]}{N^p : C : N^p + H_{\nu}},\tag{21}$$

where  $N^p = \frac{\partial F_y}{\partial \sigma}$  is the flow direction.

## 2.5.4 Mechanical equilibrium equations

The above governing equations are coupled to the mechanical equilibrium that gives the displacement field. Neglecting the body forces for a 2D solid domain  $(\Omega)$  subjected to surface force  $(t^a)$  on a portion  $(\Omega_t)$  of its boundary  $(\partial\Omega)$  and/or a displacement vector  $(u^a)$  on a boundary portion  $(\Omega_u)$ , the mechanical equilibrium equations are expressed in term of the Cauchy stress tensor  $\sigma$  as follows,

$$\nabla \sigma = \mathbf{0} \text{ in } \Omega$$
,  $\sigma \cdot \mathbf{n} = \mathbf{t}^a \text{ on } \Omega_t$ , and  $\mathbf{u} = \mathbf{u}^a \text{ on } \Omega_u$ . (22)

#### 2.6. Details of numerical simulations and material properties

We applied the "Fully Coupled" approach so that the nonlinear equations describing the solution is a single large system where all the field variables and their coupling terms are solved at once within the same iteration. It converges more robustly and uses less iterations than the "Segregated" method which solves the unknowns sequentially within a single iteration. Within each iteration, the nonlinear system of equations is linearized and solved. We also used the MUMPS "Direct" algorithm solver which is more robust and general than the "Iterative" solver which converges slower for ill-conditioned problems, such as those with a very high geometric aspect ratio and/or a high gradient in material properties. The size of the study domain is  $0.25 \times 0.25 \ \mu m^2$ , and we use free quadratic triangular elements with a minimum mesh size of 1 nm

and a maximum mesh size of 5 nm to discretise the domain. We have chosen this range to accurately capture the all-possible features of TMPT and the tetragonal-monoclinic interface. This mesh is small enough to provide the details and results similar to MD simulations [55] while allowing the use of larger sample size and smooth response that can be related to macroscopic results and experimental tests. The governing equations are solved using the input parameters given in Tables 1 and the elastic constants of the monoclinic and tetragonal phases in Table 2.

Table 1. Material properties and simulation parameters for 3Y-STZ (at. %).

Model parameter	Value			
Kinetic coefficient M (m <sup>3</sup> .J <sup>-1</sup> .s <sup>-1</sup> )	1 *			
Gradient energy coefficient $\beta$ (J.m <sup>-1</sup> )	1x10 <sup>-8</sup> [27]			
Latent heat Q (MJ.m <sup>-3</sup> )	108.8 [56]			
Energy coefficient parameter k <sub>2</sub>	2*			
Equilibrium temperature $T_0$ (K)	883 [56]			
Mass density ρ (kg.m³)	6100 [57]			
Thermal conductivity λ (W.m <sup>-1</sup> .K <sup>-1</sup> )	3 [57]			
Specific heat $C_p$ (J.kg <sup>-1</sup> .K <sup>-1</sup> )	600 [57]			
Initial yield stress σ <sub>0</sub> (MPa)	2500 [58]			
Isotropic hardening modulus $H_y$ (GPa)	50 [28]			
Thermal coefficient (K/MPa)	1.0 [59]			
Eigen strain for variant 1	$\boldsymbol{\varepsilon}_1^{00} = \begin{pmatrix} 0.0419 & 0.0761 \\ 0.0761 & -0.0181 \end{pmatrix} [60-62]$			
Eigen strain for variant 2	$\boldsymbol{\varepsilon}_2^{00} = \begin{pmatrix} 0.0419 & -0.0761 \\ -0.0761 & -0.0181 \end{pmatrix} [60-62]$			

<sup>\*</sup> These parameters are adjusted to reproduce the transformation stress reported in [58].

Table 2. Elastic properties of the tetragonal and monoclinic phases.

Parameter	$C_{II}$	C33	$C_{I3}$	C44
Phase	(GPa)	(GPa)	(GPa)	(GPa)
Monoclinic [63, 64]	361	264	62	59
Tetragonal [64, 65]	327	258	55	100

### 3. Results and Discussions

Based on previous MD simulations [26] and experimental observations [28, 66], we select three single crystals (SC): [101] orientated (SC[101]) where only transformation was observed, [001] orientated (SC[001]) where both TMPT and plasticity were reported, and [100] orientated (SC[100]) where only plasticity was observed. We considered various size, shape, orientation, and distribution of voids, shown in Figure 2, where all elliptic voids have a short semi-minor axis of 10 nm. All the simulations consist of pseudoelastic cycles operated at  $T_L = 905$  K, i.e., 22 K above the equilibrium temperature,  $T_0$ . A maximum compressive or tensile stress of 2 GPa is applied linearly during a ramp of 1.0  $\mu$ s, followed by a complete unloading to 0 MPa during another linear ramp of 1.0  $\mu$ s.

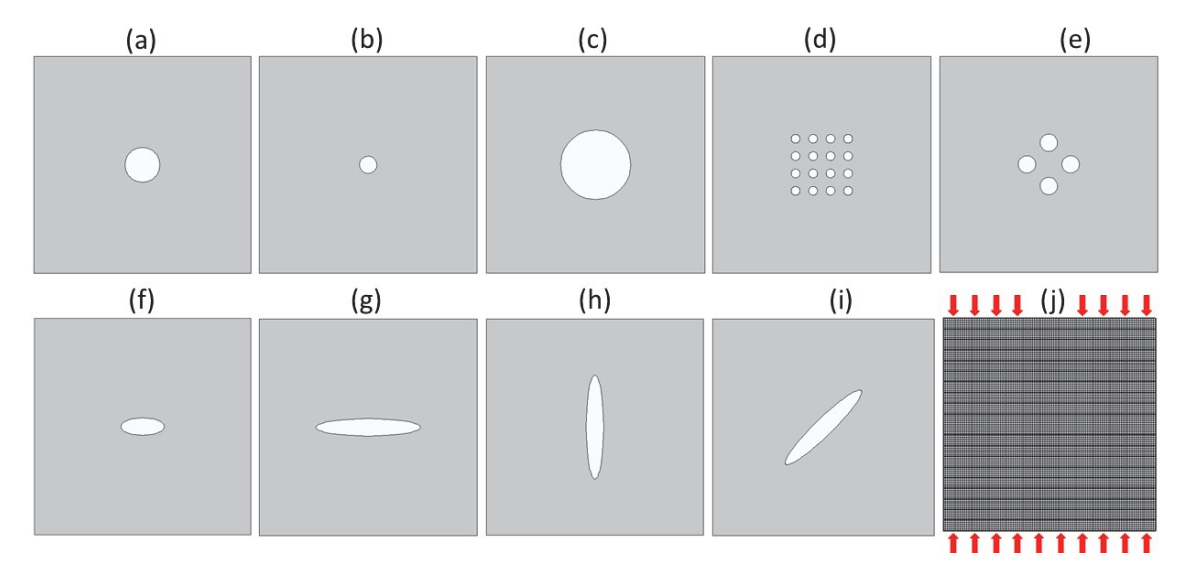


Figure 2. Square simulation samples of side length 250 nm, with (a) a circular void of 40 nm diameter (c40) which is taken as the reference sample, (b) a circular void of 20 nm diameter (c20), (c) a circular void of 80 nm diameter (c80), (d) patterned circular voids of 10 nm diameter (c10p), (e) patterned circular voids of 20 nm diameter (c20p), (f) an elliptic void with horizontal semi-major axis of 25nm (e25h), (g) an elliptic void with horizontal semi-major axis of 60 nm (e60h), (h) an elliptic void with vertical semi-major axis of 60 nm (e60v), (i) an elliptic void with diagonal semi-major axis of 60 nm (e60d), and (j) meshed defect-free bulk specimen (BS) under compression using 10,000 quadratic elements of size 2.5 nm.

### 3.1 Defected SC[101] single crystal

We first study the behavior of single crystalline 3Y-STZ having an orientation angle [101] with respect to the vertical loading direction by applying a rotation of 45° to the eigen strain tensors and stiffness matrices. In Figure 3, we compare the results for the defect-free bulk sample (BS) to the defected reference specimen with a circular void of 40 nm diameter (c40). Similar to our previous work [27], only phase transformation occurs for this crystal orientation even in the presence of void. This is demonstrated by the absence of residual strain in the stress-strain curve in Figure 3a after unloading. This curve, along with the evolution of the total surface-averaged volume fraction of monoclinic phase in Figure 3b, highlights a noticeable asymmetry of the deformation of both BS and c40 samples. This quantitative analysis of TMPT in Figure 3b reveals an initial negligible increase in the monoclinic volume fraction, followed by a rapid increase between points P1 and P2, then a modest increase toward near saturation until point L (maximum stress).

For all samples, the stress-strain curves in tension exhibit a flatter stress plateau and a lower CTS in tension (440 MPa for c40) than in compression (520 MPa for c40). This means that the 3Y-STZ is more deformable in tension with a larger hysteresis loop than in compression. This latter point is also visible in Figure 3b where a higher fraction of monoclinic phase is obtained in tension (0.93 for c40) than in compression (0.88 for c40). These results are consistent with the experimental data reported by Liu and Chen [67] where both Mg-PSZ and 3Y-STZ show an asymmetric behavior with a ratio of CTS, located at P1 in the Figure 3a, for tension over compression between 2/3 and ½. In our work, the saturation stress, located at P2 in the Figure 3a where most of TMPT is complete, in tension (610 MPa) and in compression (-810 MPa) generates an asymmetry ratio of nearly 2/3. In addition, we have stress concentration factors for c40 in tension of 2.96, 11.9, and 8.96 at points P1, P2 and L, respectively. From a theoretical perspective where the stress concentration factor is 3, we see a good agreement of this analytical value with the tensile elastic regime (P1), while those in the inelastic regime (P2 and L) diverge from the analytical value. However, the asymmetry of the degree of transformation is 1.06 meaning that its higher in tension than in compression.

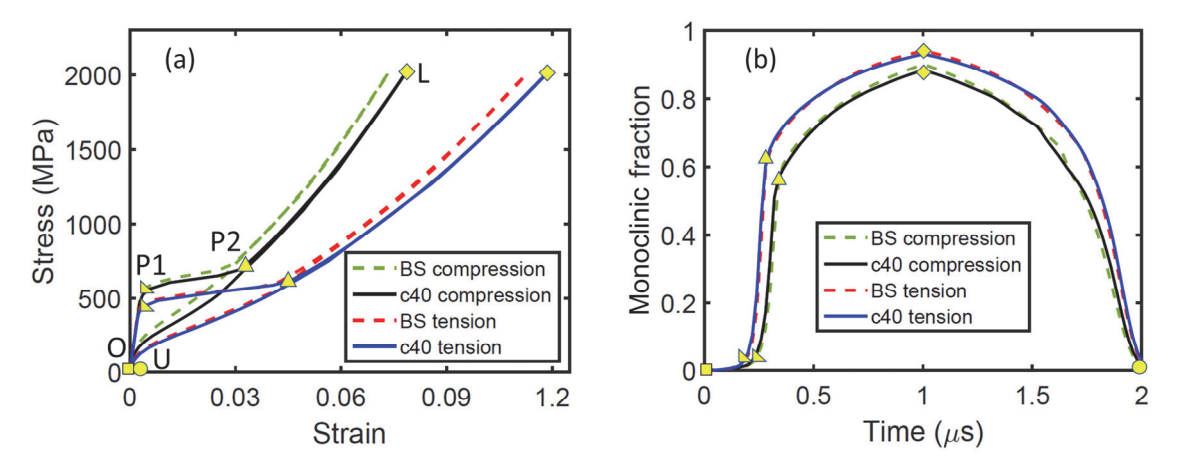


Figure 3. a) Tension and compression asymmetric stress-strain curves, and b) evolution of the monoclinic volume fraction during a pseudoelastic cycle in SC[101].

The slightly lower CTS in c40 than BS is due to the void acting as an additional nucleation

site phase transformation, where a high local stress concentration builds up and triggers the TMPT at the early deformation stage at point P1 in Figure 4. It can be also noticed that the monoclinic bands and the interfaces between the variants lay at an angle  $\pm \pi/4$  with respect to the loading direction. Likewise, by setting the applied load to generate a maximum von Mises stress of 2000 MPa, we see a maximum stress zone (MSZ) (stress ≥2000 MPa) that is surrounded by  $\pm \pi/4$  lines. As the deformation proceeds, the MSZ does not correlate with the transformation bands especially at high-load regimes (points P2 and L). The reason, which also explains the asymmetry, is that the transformation energy is related to the eigen strains. One could simplify the transformation criteria for a given variant as  $\tilde{\sigma}$ :  $\varepsilon^{00}=E_c$  where  $E_c$  is the critical energy needed to destabilize the tetragonal phase and is  $\tilde{\sigma}$  the local stress tensor. By applying the rotation of  $\pi/4$ , the new eigen strain tensors read  $\varepsilon_1^{00} = \begin{pmatrix} -0.0642 & 0.030 \\ 0.030 & 0.088 \end{pmatrix}$  and  $\mathbf{\epsilon}_{2}^{00} = \begin{pmatrix} 0.088 & 0.030 \\ 0.030 & -0.0642 \end{pmatrix}$ . Thus, under pure uniaxial compression along y-axis, the dominant term of the transformation energy would come from the variant 2 as  $-0.0642(-|\sigma_{22}|)$ , while under pure uniaxial tension it will come from variant 1 as  $+0.088|\sigma_{22}|$ . Hence variant 1 is favored in tension and variant 2 is predominant in compression. Likewise, the amount of stress required to reach  $E_c$  is lower in tension than in compression (see Figure 4). We attribute the lower asymmetry in c40 than BS to the presence of circular void that absorbs the hydrostatic part of the eigen strain and mitigate the TMPT-induced volume expansion. The results unravel that asymmetry mechanisms in 3Y-STZ are rooted from the non-deviatoric nature of the Bain tensors.

Since ceramics are mainly used in compressive loading conditions, the study of further effects, such as size, shape, and distribution of the defects, will be conducted in compression only.

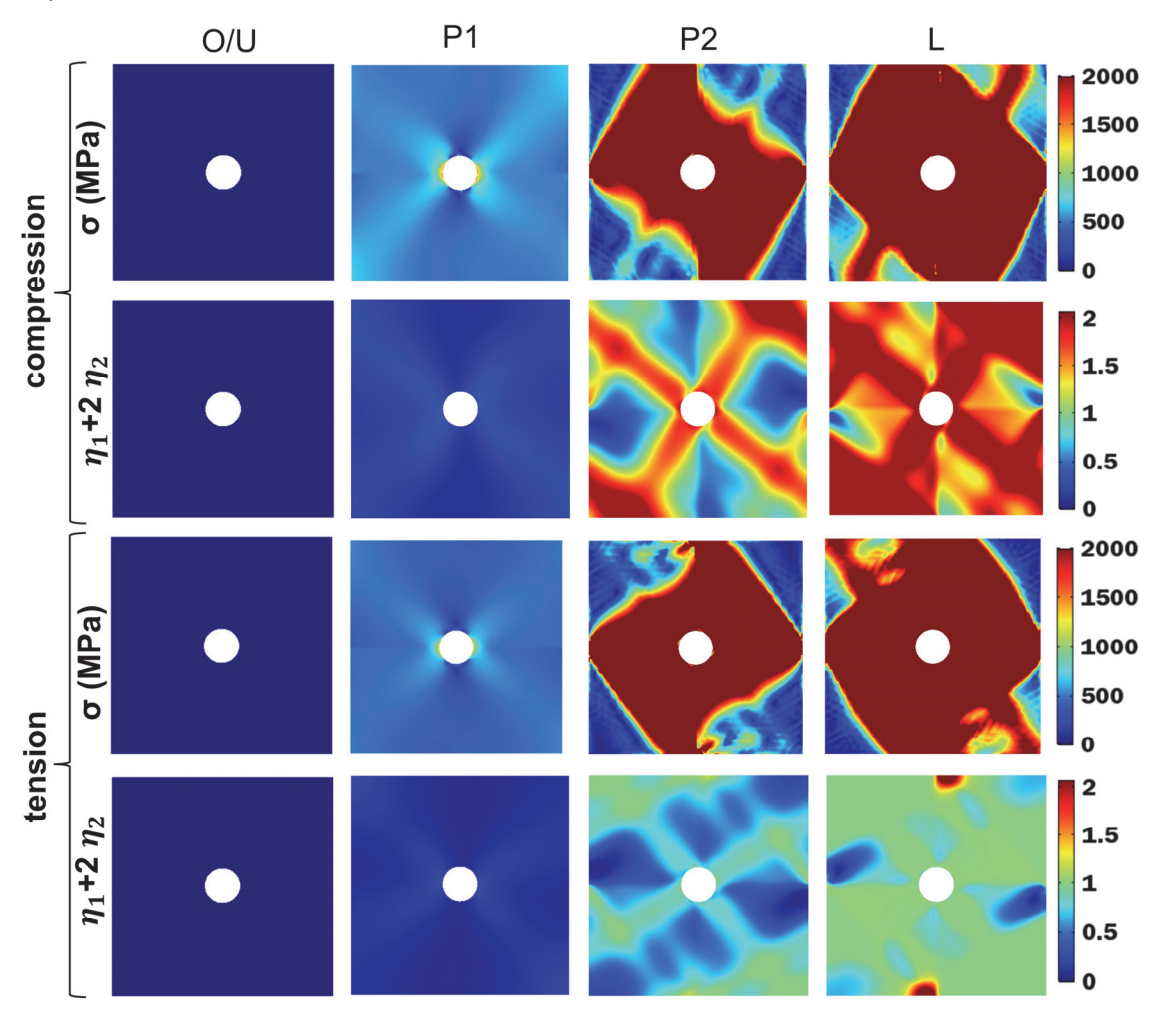


Figure 4. Distribution of stress and evolution of the monoclinic phase in c40 during compressive and tensile deformation of SC[101].

### 3.1.1 Effect of void size and distribution

Here we consider two additional specimens with void diameter of 20 nm (c20) and 80 nm (c80) to study the effects of void size on the overall stress-strain response. The stress-strain curves in Figure 5a show that as the diameter of void increases, the CTS decreases from 540 MPa for c20 to 520 MPa for c40, and to 440 MPa for c80, and the materials increasingly softens. One of the reasons would be the boundary effects as the diameter increases; hence, a longer stress plateau and larger hysteresis loop are obtained for c80. The similar results of c20

and c40 cases suggest that a smaller diameter would results in flaw tolerance and void-insensitive strength [9]. Figure 5b shows that by keeping the same void fraction and only changing density in patterned distributions with diameters of 10 nm (c10p) and 20 nm (c20p), the stress strain curves display slightly different hysteresis size. This can be explained by the presence of a high transformation zone between the voids in c10p and c20p (see Figure 5d). However, in all these specimens, the interface of the variants lays on the plan having an angle  $\pm \pi/4$ . It is worth emphasizing the increase in the forward TMPT degree and reduction of the high stress zone (HSZ) where its value is higher than or equal to the applied stress of 2 GPa, as the void diameter increases from 20 nm to 40 nm and then to 80 nm, seen in Figure 4 and Figure 5c. The stress and TMPT distribution in Figure 5d show that changing the distribution of voids does not affect the deformation mechanism except in the saturation stage (Figure 5b) where c40 has a steeper slop than c10p and c20p.

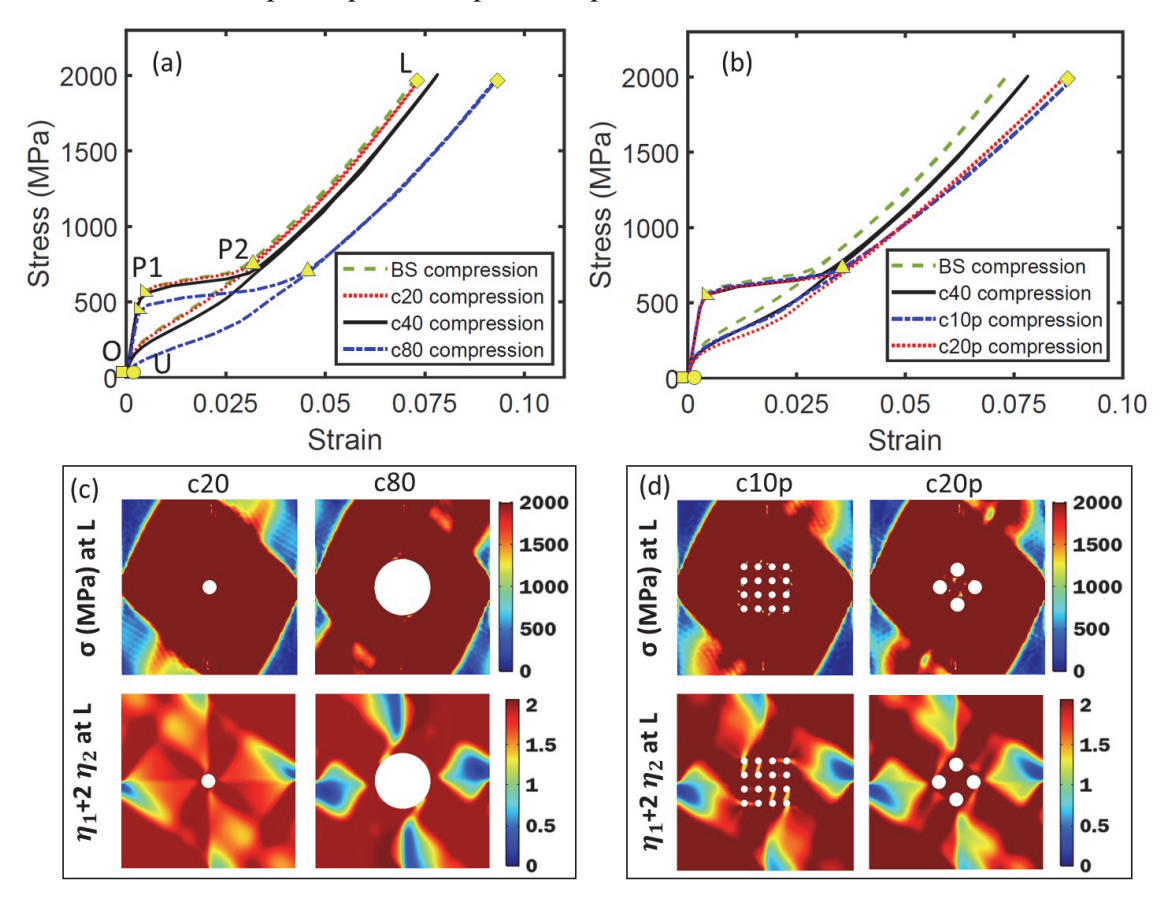


Figure 5. a) Compressive stress-strain curves for different circular void sizes, b) compressive stress-strain curves for different void distribution with the same void fraction, and c) distributions of stress and monoclinic phase at the end of loading for c20 and c80, and d) for different distribution of voids in SC[101].

## 3.1.2 Elliptic voids

We study the effect of defect shape by using elliptic voids with semi-major axis 25 nm aligned in the horizontal (e25d), vertical (e25v) and diagonal (e25d) directions and elliptic voids with semi-major axis of 60 nm (e60h, e60v, and e60d). The results in Figure 6 show negligible difference between c40, e25h, e25v and e25d with CTS of about 520 MPa, possibly due to their "quasi-circular" shapes. However, visible variations can be noticed between e60h, e60v and e60d, both in terms of CTS (400 MPa, 420 MPa and 540 MPa, respectively) and hysteresis size. Figure 6d shows that e60h generates more transformation than e60h and e60v.

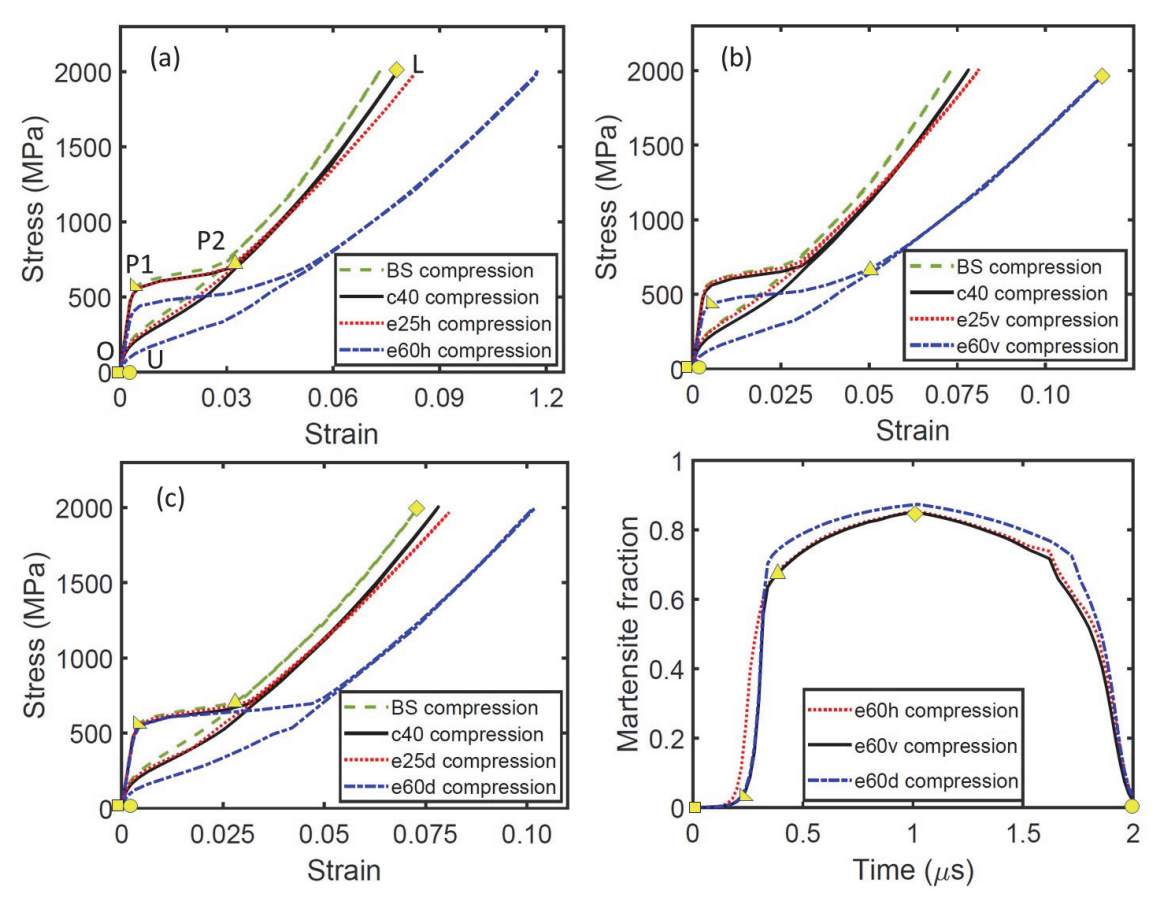


Figure 6. Comparison of the compressive stress-strain curves of elliptic voids a) e25h and e60h, b) e25v and e60v, and c) e25d and e60d with BS and c40 samples, and d) evolution of the average monoclinic phase in e60h, e60v and e60d in SC[101].

Assuming that crack propagates and/or pores coalesce after saturation of transformation, the stress intensity factor could be approximated as [68]:

$$K_I = \sigma_s Y \cos(\chi) \sqrt{\pi a} , Y = \sqrt{\sec\left(\frac{\pi a}{2W}\right)},$$
 (23)

where  $\sigma_s$  is the saturation stress and  $\chi$  is the orientation angle of long axis of the elliptic defect of length a. Therefore, the stress intensity factor is 5.6 MPa.m<sup>1/2</sup> for the e60d, 7.4 MPa.m<sup>1/2</sup> for e0h, and 0 MPa.m<sup>1/2</sup> for e60v. The stress intensity factor of e60d with an orientation  $\pm \frac{\pi}{4}$ , being an average representation of the various angles, agrees well with the room temperature experimental data of Casellas et al. [36] with the stress intensity factor of 3.9 MPa.m<sup>1/2</sup>, 5.0 MPa.m<sup>1/2</sup> and 5.8 MPa.m<sup>1/2</sup> for the as-sintered, heat-treated for 2 hours, and heat-treated for 10 hours 2.5Y-STZ specimens, respectively. Vasylkiv et al. [69] reported a fracture toughness between 7.2 and 9.2 MPa.m1/2 for as-sintered 3Y-STZ, which correlates well with our simulation result for e0h. In addition, the calculated stress concentration factor at points P1 and L for e60h in tension are 13.06 and 20.3, respectively. Here again, the stress concentration factor of the elastic regime agrees well with the analytical value [70] reading  $1 + 2 \times \frac{major\ axis}{minor\ axis}$  $=1+2\times\frac{60}{10}=13$  . These results can be understood from the distribution of stress and monoclinic phase in Figure 7. While the maximum stress is always located at the ellipse vertices, the alignment of the long axis of e60d at  $\pi/4$  plays in favors of its higher transformation since the transformation bands and interfaces are in the  $\pm \pi/4$  plane. In can be seen that additional transformation bands appear at the vertices of e60d (with dashed circles) contrary to e60h and e60v. However, the localization of the HSZ on the  $\pm \pi/4$  plan in SC[101] generates less stress concentration in e60d, which explains its higher onset stress.

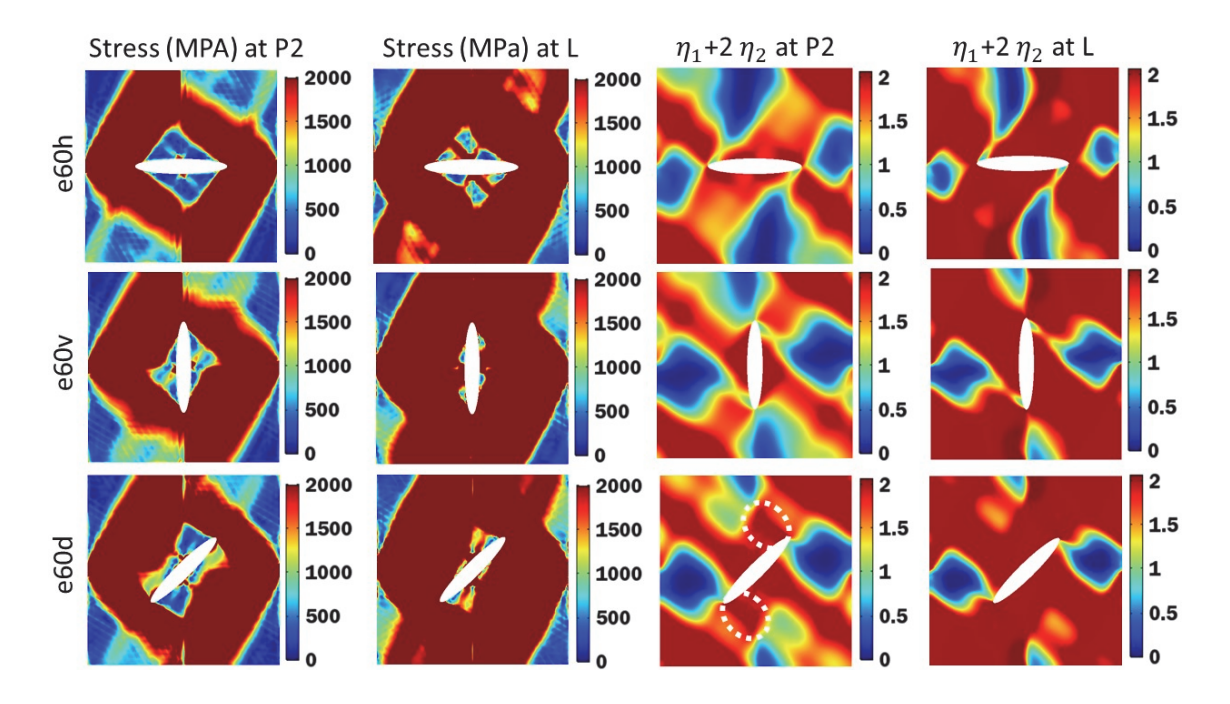


Figure 7. Distributions of stress and monoclinic phase at P2 and L for different orientations of the elliptic void in SC[101]. Additional bands in e60d are indicated with dashed circles.

## 3.2 Defected SC[001] single crystal

In this section, we present and discuss the simulation results for the single crystal with an orientation angle of [001] with respect to the vertical loading direction by applying a rotation of 90° to the eigen strain tensors and stiffness matrices. The compressive stress-strain curves in Figure 8a with pure linear elastic unloading confirmed that only plasticity occurs in both BS and c40. However, due to the stress concentration building up around the void, the yield stress is lower for c40 (1400 MPa) than for BS (1520 MPa). This explains the larger plastic strain in c40 than BS. However, in tension, the specimens display both transformation and plasticity. To elucidate this chain of events, we notice that a rotation of 90° generates the new Bain strain tensors  $\varepsilon_1^{00} = \begin{pmatrix} -0.0181 & -0.0761 \\ -0.0761 & 0.0419 \end{pmatrix}$  and  $\varepsilon_2^{00} = \begin{pmatrix} -0.0181 & 0.0761 \\ 0.0761 & 0.0419 \end{pmatrix}$ . The dominant transformation energy term reads -0.0419 $|\sigma_{22}|$  (negative and thus always  $< E_c$ ) under uniaxial compression, and  $+0.0419|\sigma_{22}|$  in uniaxial tension, which explains the absence of TMPT in compression and the presence of TMPT in tension. Besides, because the plastic driving force in Eq. 13 is maximum for this orientation, both tensile and compressive samples display plastic deformation. However, the tensile yield stress is less than the compressive one because of the local stress effects of TPMT. The tensile CTS is also lower for c40 (770 MPa) than for BS (920 MPa), like the compressive SC[101] sample.

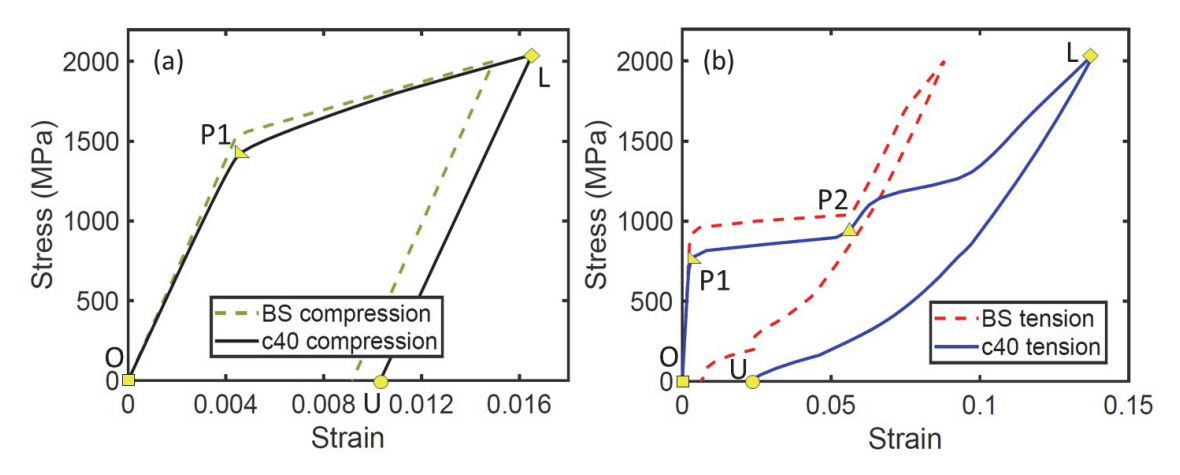


Figure 8. Comparison of the stress-strain curves of c40 with BS under (a) compression and (b) tension in SC[001].

The confinement of the plastic gliding around the void generates a butterfly plastic zone with wings pointing towards the vertices of samples (see the first column of Figure 9), which provides incentives to understand the stronger hardening in c40 compared to BS (Figure 8). The second column of Figure 9 confirms the absence of transformation in c40 for this specific crystal orientation. For the tensile specimen, the distribution of the equivalent plastic strain shows dendritic-like bands touching the voids, rather than a butterfly shape. This larger plasticaffected zone explains the higher residual strain of c40 in tension than in compression in Figure 8. The positive shear term in eigen strain tensor of variant 2 increases its stability over variant 1 and explains its predominance in Figure 9. The deflection noted between P2 and L in Figure 8b corresponds to partial reorientation of variant 2 into variant 1 highlighted by the white dashed ellipse in the last column of Figure 9. When transformation appears for this crystal orientation, they are arranged in vertical bands with interfaces laying along [001] direction. Comparing the last two columns for point U in Figure 9, we can see that the residual monoclinic phase is trapped between the plastic bands. Since we have properly enforced the loadingunloading conditions contrary to other PFMs [71, 72], in Eq. 12, no change is noted in the plastic strain distribution between L and U.

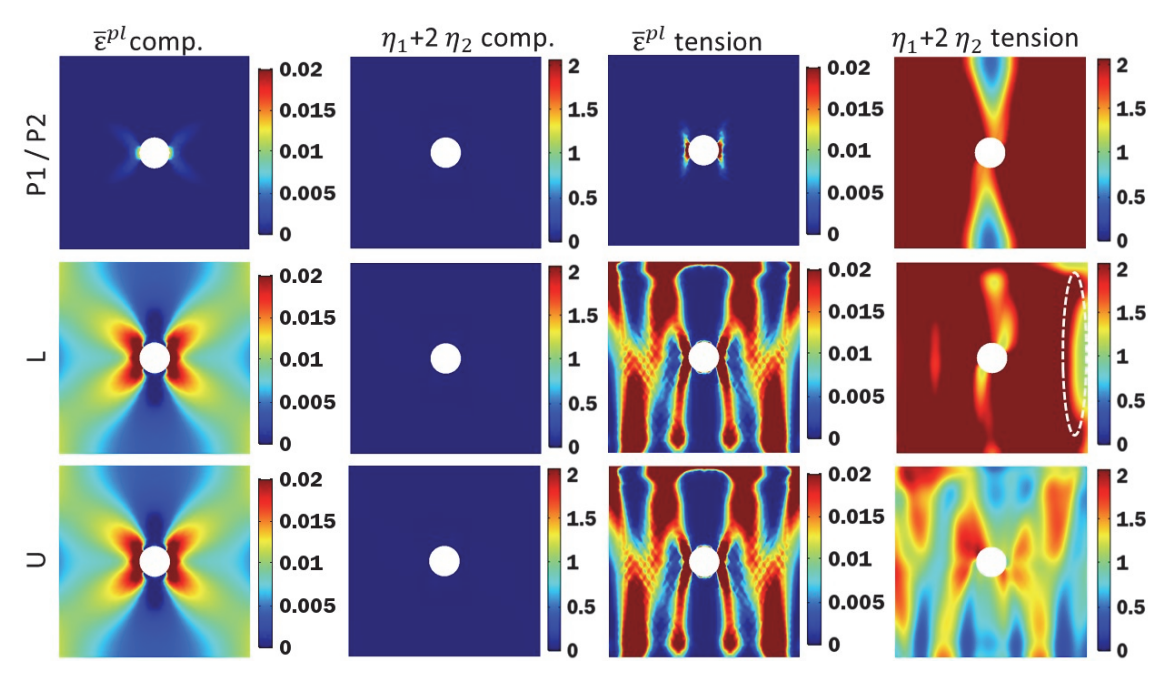


Figure 9. Distributions of equivalent plastic strain and monoclinic phase at points P2, L and U for c40 in compression and tension in SC[001]. Partial reorientation of variant 2 into variant 1 is highlighted by a white dashed ellipse.

# 3.2.1 Effect of void size and distribution

We study the size effect using c80 and the void distribution effect using c20p. The results in Figure 10 shows lower yield stress for c80 (1100 MPa). Despite having nearly, the same yield stress than c40, a noticeable difference is observed between their plastic hardenings, which causes lower plastic strain in c20p (0.8%) than in c40 (1.0%). Such results can be explained by the plasticity of the area enclosed between the four circles of c20p (Figure 10b) that favors local effects. Likewise, the lower yield stress and hardening in c80 explains its larger plastic strain (1.8%) than c40. However, the variation of the void size and distribution did not trigger TMPT (Figure 10b).

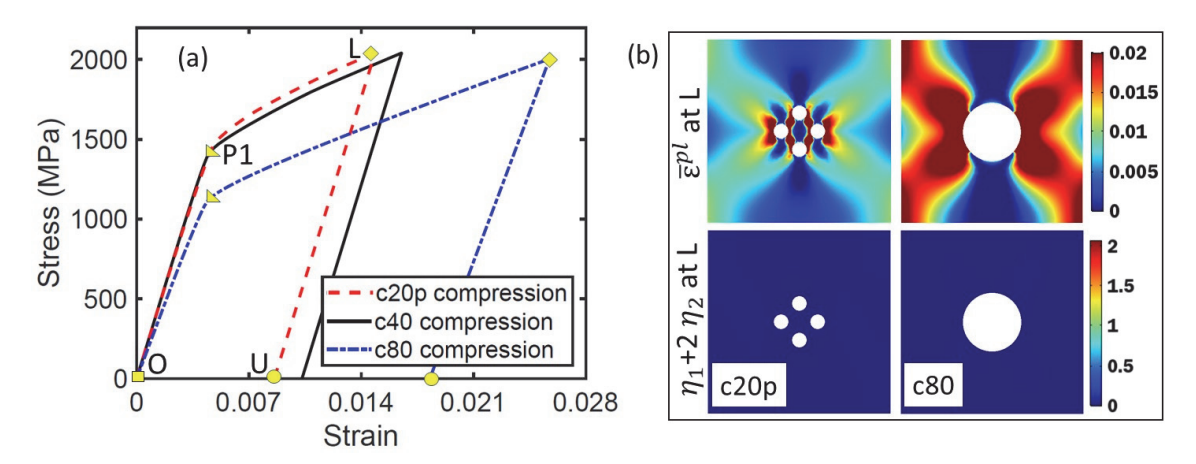


Figure 10. (a) Comparison of the compressive stress-strain curves of c80 and c20p with c40, and (b) distributions of equivalent plastic strain and monoclinic phase therein at point L in SC[001].

## 3.2.2 Elliptic voids

Based on the results of SC[101] in section 3.1, we focus here only on e60h, e60v and e60d SC[001] samples. The results in Figure 11 show significant dependence of the stress-strain curves on orientation of the major axis of ellipse. The yield stress and equivalent plastic strain are respectively 920 MPa and 2.6% for e60h, 1480 MPa and 0.96% for e60v, and 1100 MPa and 1.7% for e60d.

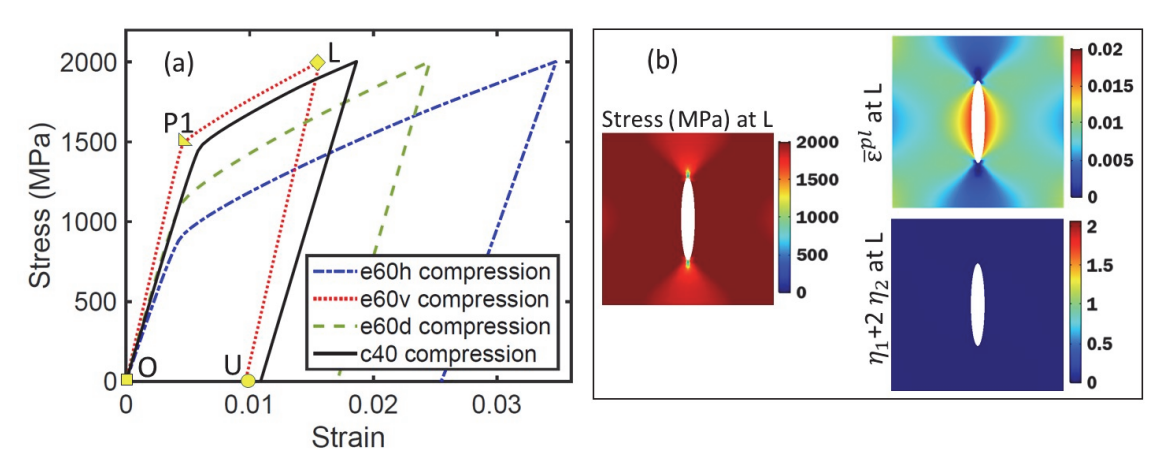


Figure 11. (a) Comparison of the stress-strain curves of e60h, e60v and e60d with c40, and (b) distributions of von Mises stress, equivalent plastic strain and monoclinic phase in e60v at point L in SC[001].

The stress distribution in e60h and e60d in Figure 12 shows that the central zone covering the width of the ellipse does not carry out the load due to the presence of void. The plastic zone has butterfly shape with a larger size for e60h due its strong hindering on the load

transfer than e60d, which explains its larger residual strain at point U. A striking difference is that contrary to e60v in Figure 11b, e60h and e60d show parasitic TMPT after loading at point L, part of which remains trapped by the plastic deformation after unloading at point U. Such interesting finding can be related to the local positive axial and shear stresses concentration around the ellipse vertices (Poisson effects) which is large enough in SC[001] to trigger the apparition of variant 1. Because most of this parasitic TMPT is trapped by the high plastic zone, no effect is observed in the corresponding stress-strain curves in Figure 11a.

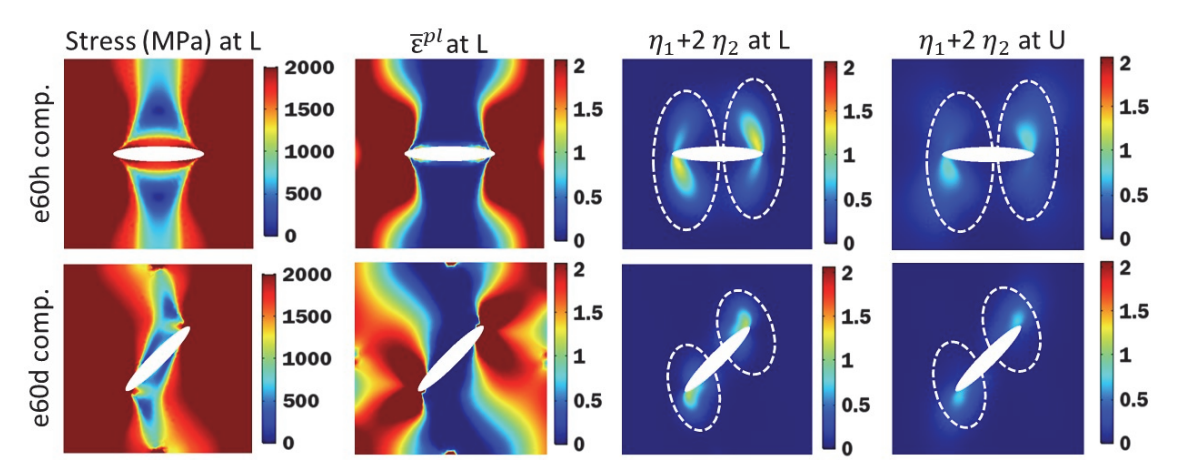


Figure 12. Distributions of von Mises stress, equivalent plastic strain and monoclinic phase at points L and U for e60h, and e60d in SC[001]. The dashed circles show presence of TMTP in defect SC[001] contrary to the bulk SC[001] studied in [27].

# 3.3 Defected SC[100] single crystal

In this section, we present and discuss the simulation results for the defected single crystal having an orientation angle of [100] with respect to the vertical loading direction by applying a rotation of  $0^{\circ}$  to the eigen strain tensors and stiffness matrices. For this specific case, both plasticity and TMPT were reported in our previous work [27] during compression of the bulk sample. For the defected sample, Figure 13a shows a combination of transformation and plasticity under compression, and only plasticity in tension, which are the opposite of those of SC[001] in the section 3.2. A major difference is that the curves in Figure 13a do not exhibit distinct portions between TMPT and plasticity. This due to the higher CTS for this crystal orientation. In fact, by applying a rotation of  $0^{\circ}$ , the Bain strain tensors remain  $\varepsilon_1^{00} = \begin{pmatrix} 0.0419 & 0.0761 \\ 0.0761 & -0.0181 \end{pmatrix}$  and  $\varepsilon_1^{00} = \begin{pmatrix} 0.0419 & -0.0761 \\ -0.0761 & -0.0181 \end{pmatrix}$ . Therefore, the compressive transformation energy can be approximated as  $0.0181|\sigma_{22}|$  for both monoclinic variants, with variant 2 being favoured by its negative shear terms. Thus, much more stress is required to

reach the critical energy  $E_c$  compared to the other orientations. The critical TMPT stress is 1390 MPa for c40 and 1560 MPa for BS. The values are so close to the yield stress that no distinction is possible between the two mechanisms. However, in tension, this transformation driving force becomes -0.0181 $|\sigma_{22}|$ , which explains the absence of TMPT in tensile loading. While the residual plastic strain is 0.1% like c40 in compressive SC[001], the variation of the elastic stiffness explains the larger strain in SC[100] at point L.

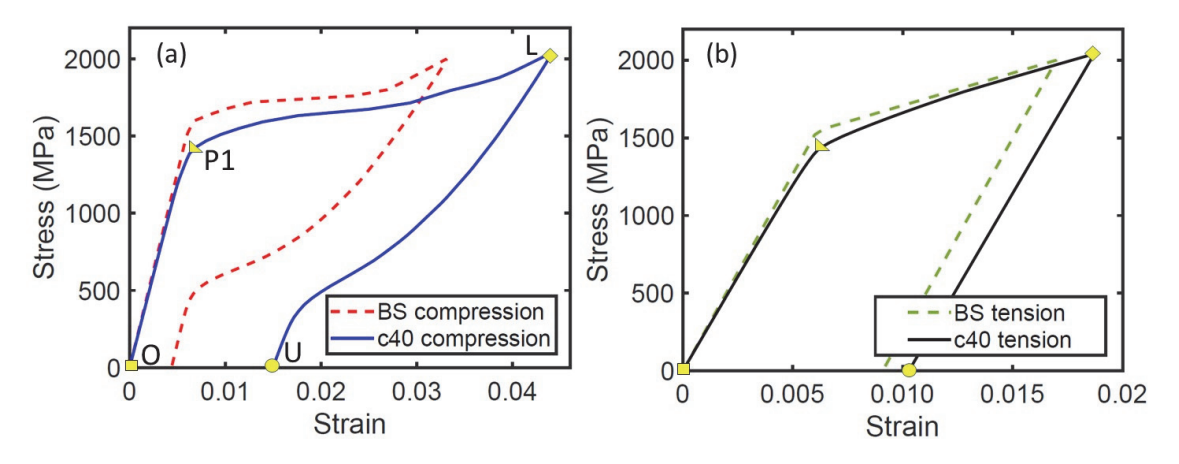


Figure 13. Comparison of the compressive stress-strain curves of c40 with BS (no voids) under (a) compression and (b) tension in SC[100].

Figure 14 shows monoclinic phase with horizontal interfaces, where the high stress creates horizontal plastic bands in compression, even if a butterfly-like plastic zone is noticed near the circular void. However, in tension, there is only plasticity with butterfly zone shape, and no substantial TMPT, even there is some trace of monoclinic phase at the end of the loading. A striking difference however is that contrary to compression of SC[001], tensile deformation of c40 in SC[100] displays slight phase transformation, shown in the zoom-in topography in the 4<sup>th</sup> column of Figure 14. Since TMPT occurs in a catalytic way in single crystals, the lower amount of monoclinic phase suggest that it has appeared near the end of loading, i.e. after initiation of plasticity, which may have hindered its subsequent evolution.

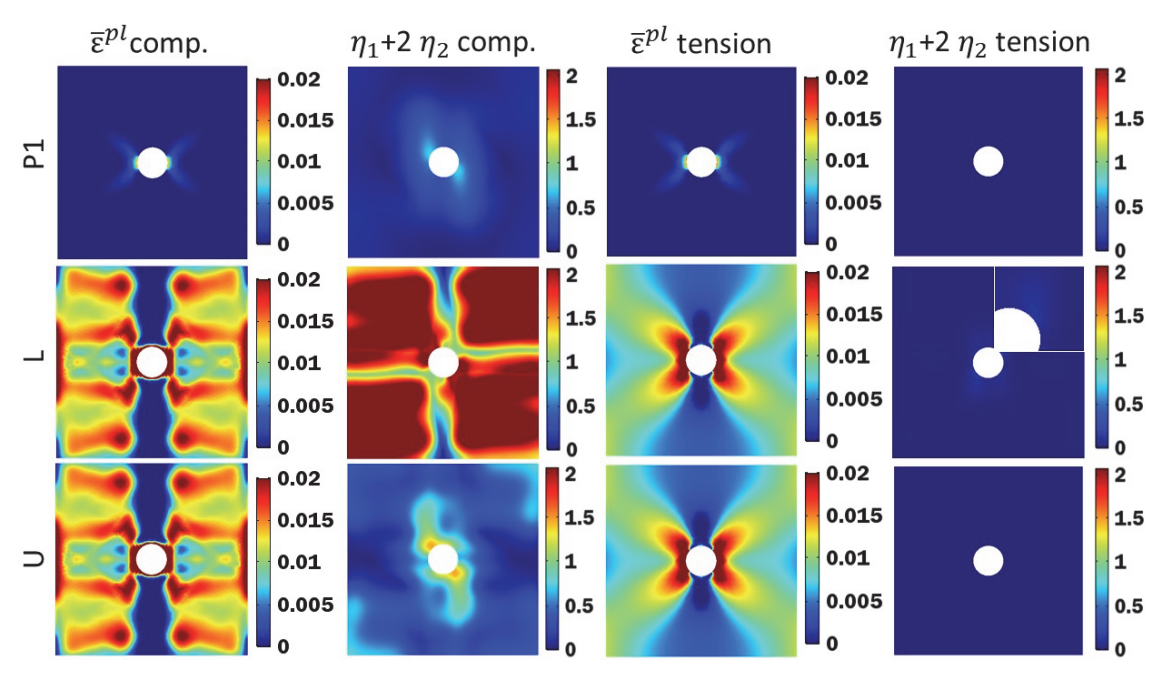


Figure 14. Distributions of equivalent plastic strain and monoclinic phase a points L and U for c40 in compression and tension in SC[100].

## 3.3.1 Elliptic void

Considering elliptic voids with 60 nm semi-major axis generates different results illustrated in Figure 15. The CTS in Figure 15a is lower for e60h (980 MPa) than c40, e60v (1520 MPa) and e60d (1420 MPa). The insets in Figure 15b highlight horizontal transformation bands and plastic zones, the latter being located at the interface. The suggest possible interface fracture in 3Y-STZ. These fine strips of high plastic zone pin TMPT and cause some residual monoclinic phase after unloading.

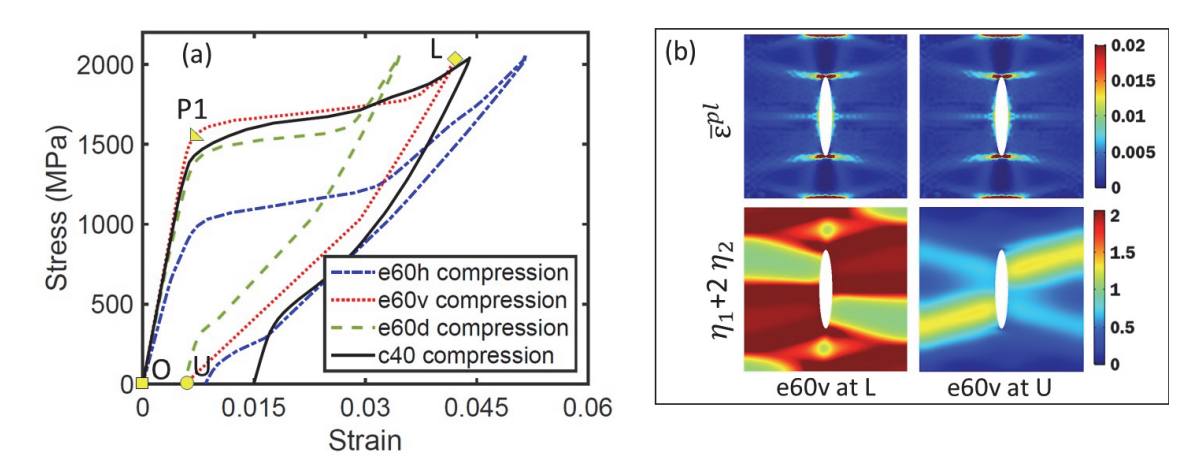


Figure 15. Comparison of the compressive stress-strain curves of e60h, e60v and e60d with

c40 (a), and distributions of von Mises stress, equivalent plastic strain and monoclinic phase at point L in e60v (b) in SC[100].

The distribution of stress, equivalent plastic strain and monoclinic phase in e60h and e60d in Figure 16 show that phase transformation and plastic deformation occur in mainly in HSZ for these samples which maximum plasticity always occurring at the ellipse vertices, which in turn prevents from complete shape recovery and complete reverse transformation.

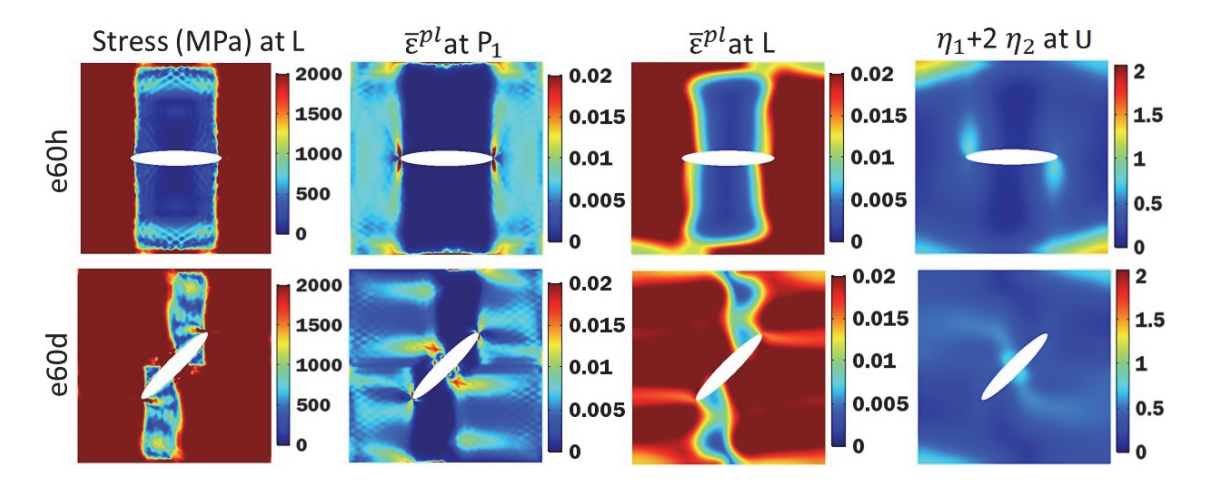


Figure 16. Distributions of von Mises stress, equivalent plastic strain and monoclinic phase a points L and U for e60h, and e60d in SC[100].

### 3.4 Deformation modes

The deformation mode of the samples c40, e60h, e60v, and e60d are shown in Figure 17 for the three single crystals SC[101], SC[001] and SC[100]. For SC[101] all samples have the same compressed shape that reminds the third deformation mode of a cantilever beam. For SC[001], all specimens have a compressed shape like the second deformation mode of a cantilever beam. However, SC[100] samples exhibit different compressed shape due the simultaneous occurrence of TMPT and plasticity and its lower elastic modulus along the loading direction. The second row highlights that presence of only plasticity does not affect the void, which can be explained by the volume conservation during plastic deformation. However, the volume expansion accompanying TMPT induces visible effects on the deformation mode and evolution of the void. In e60h, the void nearly disappears after compression induced TMPT, while in e60v, the volume expansion opens the crack. For c40, also the TMPT displays partial closure but less than in e60h, even if it is better than in e60v. This renders possible to develop in 3Y-STZ a high capacity to accommodate their TMT-induced volume expansion sand thus carry more fatigue lifetime, especially in the high cycle regime.

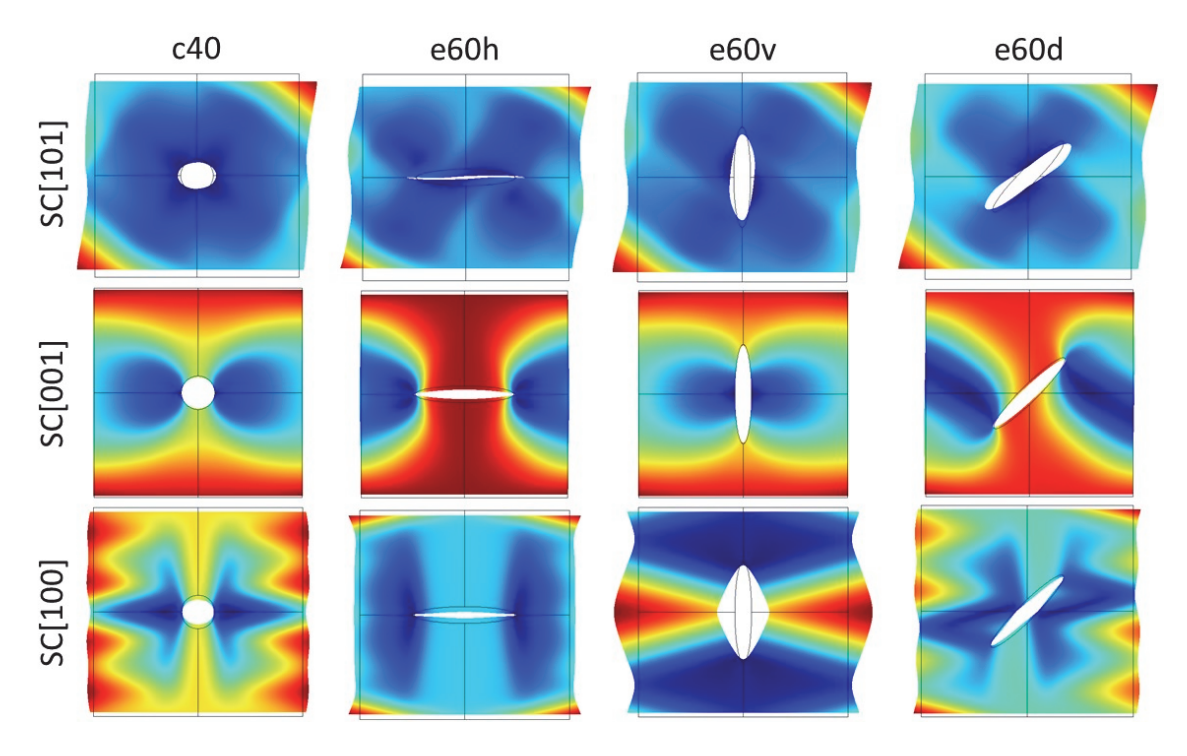


Figure 17. Deformation modes of c40, e60h, e60v and e60d in SC[101], SC[001] and SC[100] at point L.

### 4. Conclusion

We used an elastoplastic phase-field model to investigate the deformation mechanisms of defected 3Y-STZ considering circular and elliptic voids with different size, orientation, and distribution. Our findings unravel the characteristics of static defect behavior and their effects on asymmetrical mechanical behavior of 3Y-STZ in tension and compression.

Results point to a high dependency of the mechanical behavior of samples on their crystal orientation. In SC[101] specimen, only transformation is observed both in tension and compression, irrespective of the defect characteristics. However, the critical transformation stress, the average volume fraction of monoclinic phase and the size of hysteresis loop change drastically by increasing the diameter of circular void or the orientation of elliptic void. We found that the tension-compression asymmetry of the TMPT features (e.g., critical stress, hysteresis size, activated variant, and degree of transformation) is linked to the activation of different monoclinic variants. In SC[001], only plasticity is observed in compression but both TMPT and plasticity are activated in tension, with different shape of the plastic zone in compression (butterfly shape) and tension (dendritic-like shape). In addition, parasitic TMPT is noticed for horizontal elliptic voids perpendicular to the loading direction, or diagonal elliptic

voids aligned at 45° from the loading direction. Defected SC[100] samples display simultaneous TMPT and plasticity with no distinct compressive transformation and yield stresses, and they exhibit only plasticity in tension. Presence of high plastic zone at the interface of the different variants suggests possible fracture at these locations. Comparison of the shape of different samples after compression pointed out that the volume expansion associated with TMPT can assist the crack closure for circular or horizontal elliptic voids but opens the crack for vertical elliptic voids parallel to the loading direction. In the absence of TMPT, the volume change after plastic deformation was negligible which is consistent with the isochore nature of plasticity. The knowledge of the behavior of static defects obtained from the present study will set the grounds for proper exploration of the dynamic fracture mechanisms by providing clear understanding of the energy distribution, stress relaxation, stress concentration and stress intensity ahead of the crack front. Proper investigation of interface and grain boundary fracture in 3Y-STZ samples, as well as the possible improvement of its fatigue life by mitigation of volume expansion through defect engineering will be tackled in our future research.

#### **CRediT Author Statement**

**Cheikh Cissé:** Conceptualization, Methodology, Software, Formal analysis, Writing- Original draft preparation. **Mohsen Asle Zaeem:** Supervision, Conceptualization, Methodology, Writing- Reviewing and Editing, Funding Acquisition.

### Acknowledgement

This work was supported by the U.S. National Science Foundation, under Award number 2054274. The authors are grateful for the computer time allocation provided by the Extreme Science and Engineering Discovery Environment (XSEDE) to complete the simulations.

### **Declaration of Competing Interest**

The authors declare that they have no known competing financial interests or personal relationships that could have appeared to influence the work reported in this paper.

### **Data Availability**

The datasets generated and/or analyzed in this study are available from the corresponding author on reasonable request.

#### References

- [1] K. Lu, The future of metals, science 328(5976) (2010) 319-320.
- [2] J.H. Perepezko, The hotter the engine, the better, Science 326(5956) (2009) 1068-1069.
- [3] N.P. Padture, Advanced structural ceramics in aerospace propulsion, Nature materials 15(8) (2016) 804-809.
- [4] J. Knaster, A. Moeslang, T. Muroga, Materials research for fusion, Nature Physics 12(5) (2016) 424-434.
- [5] R.O. Ritchie, The conflicts between strength and toughness, Nature materials 10(11) (2011) 817-822.
- [6] C. Cisse, W. Zaki, T.B. Zineb, A review of modeling techniques for advanced effects in shape memory alloy behavior, Smart Materials and Structures 25(10) (2016) 103001.
- [7] S. Daly, A. Miller, G. Ravichandran, K. Bhattacharya, An experimental investigation of crack initiation in thin sheets of nitinol, Acta Materialia 55(18) (2007) 6322-6330.
- [8] T. Baxevanis, C.M. Landis, D.C. Lagoudas, On the fracture toughness of pseudoelastic shape memory alloys, Journal of Applied Mechanics 81(4) (2014).
- [9] N. Zhang, M. Asle Zaeem, Nanoscale flaw tolerance behaviour of polycrystalline tetragonal zirconia nanopillars, International Journal of Mechanical Sciences 173 (2020) 105405.
- [10] N. Zhang, M. Asle Zaeem, Nanoscale self-healing mechanisms in shape memory ceramics, npj Computational Materials 5(1) (2019) 1-8.
- [11] A. Suresh, M.J. Mayo, W.D. Porter, C.J. Rawn, Crystallite and grain-size-dependent phase transformations in yttria-doped zirconia, Journal of the American Ceramic Society 86(2) (2003) 360-362.
- [12] X.M. Zeng, Z. Du, C.A. Schuh, N. Tamura, C.L. Gan, Microstructure, crystallization and shape memory behavior of titania and yttria co-doped zirconia, Journal of the European Ceramic Society 36(5) (2016) 1277-1283.
- [13] J. Chevalier, L. Gremillard, A.V. Virkar, D.R. Clarke, The tetragonal-monoclinic transformation in zirconia: lessons learned and future trends, Journal of the american ceramic society 92(9) (2009) 1901-1920.
- [14] R. Stevens, An introduction to zirconia: Zirconia and zirconia ceramics. Twickenham: Magnesium elektrum, 1986, Magnesium Elektron Publications.
- [15] M. Swain, Shape memory behaviour in partially stabilized zirconia ceramics, Nature 322(6076) (1986) 234-236.
- [16] A. Evans, A. Heuer, Transformation toughening in ceramics: Martensitic transformations in crack-tip stress fields, Journal of the American Ceramic Society 63(5-6) (1980) 241-248.
- [17] M. Mamivand, M. Asle Zaeem, H. El Kadiri, Shape memory effect and pseudoelasticity behavior in tetragonal zirconia polycrystals: A phase field study, International Journal of Plasticity 60 (2014) 71-86.
- [18] M. Rashad, H. Baioumy, Effect of thermal treatment on the crystal structure and morphology of zirconia nanopowders produced by three different routes, journal of materials processing technology 195(1-3) (2008) 178-185.
- [19] A. Lotfolahpour, M. Asle Zaeem, Effects of cleavage plane and material strength on fracture of polycrystalline brittle materials: A phase-field modeling study, Computational Materials Science 197 (2021) 110642.
- [20] S.Y. Liu, I.W. Chen, Plasticity-induced fatigue damage in ceria-stabilized tetragonal zirconia polycrystals, Journal of the American Ceramic Society 77(8) (1994) 2025-2035.
- [21] S.Y. Liu, I.W. Chen, Fatigue of Yttria-Stabilized Zirconia: I, Fatigue Damage, Fracture Origins, and Lifetime Prediction, Journal of the American Ceramic Society 74(6) (1991) 1197-1205.
- [22] B.J. Hulm, W.J. Evans, Evaluation of the Cyclic Fatigue Life of 3-mol%-Yttria-Stabilized Zirconia Bioceramic Using Biaxial Flexion, Journal of the American Ceramic Society 83(2) (2000) 321-328.
- [23] E. Wolf, Fatigue crack closure under cyclic tension, Engineering fracture mechanics 2(1) (1970) 37-45.
- [24] A. Vasudeven, K. Sadananda, N. Louat, A review of crack closure, fatigue crack threshold and related phenomena, Materials Science and Engineering: A 188(1-2) (1994) 1-22.
- [25] N. Zhang, M. Asle Zaeem, Nanoscale self-healing mechanisms in shape memory ceramics, npj Computational Materials 5(1) (2019) 1-8.
- [26] N. Zhang, M. Asle Zaeem, Competing mechanisms between dislocation and phase transformation in plastic deformation of single crystalline yttria-stabilized tetragonal zirconia nanopillars, Acta Materialia 120 (2016) 337-347.
- [27] C. Cissé, M. Asle Zaeem, A Phase-Field Model for Non-Isothermal Phase Transformation and Plasticity in Polycrystalline Yttria-Stabilized Tetragonal Zirconia, Acta Materialia 191 (2020) 111-123.
- [28] X.M. Zeng, A. Lai, C.L. Gan, C.A. Schuh, Crystal orientation dependence of the stress-induced martensitic transformation in zirconia-based shape memory ceramics, Acta Materialia 116 (2016) 124-135.
- [29] R. Dauskardt, W. Yu, R. Ritchie, Fatigue crack propagation in transformation-toughened zirconia ceramic, Journal of the American Ceramic Society 70(10) (1987) C-248-C-252.
- [30] J.F. Tsai, C.S. Yu, D.K. Shetty, Fatigue crack propagation in ceria-partially-stabilized zirconia (Ce-TZP)-alumina composites, Journal of the American Ceramic Society 73(10) (1990) 2992-3001.

- [31] S.Y. Liu, I.W. Chen, Fatigue of Yttria-Stabilized Zirconia: II, Crack Propagation, Fatigue Striations, and Short-Crack Behavior, Journal of the American Ceramic Society 74(6) (1991) 1206-1216.
- [32] G. Grathwohl, T. Liu, Crack resistance and fatigue of transforming ceramics: II, CeO2-stabilized tetragonal ZrO2, Journal of the American Ceramic Society 74(12) (1991) 3028-3034.
- [33] P. Cao, T. Liu, C. Pu, H. Lin, Crack propagation and coalescence of brittle rock-like specimens with pre-existing cracks in compression, Engineering geology 187 (2015) 113-121.
- [34] S. Park, J. Kim, M. Kim, H. Song, C. Park, Microscopic observation of degradation behavior in yttria and ceria stabilized zirconia thermal barrier coatings under hot corrosion, Surface and Coatings Technology 190(2-3) (2005) 357-365.
- [35] R. Govila, Strength characterization of yttria-partially stabilized zirconia, Journal of materials science 30(10) (1995) 2656-2667.
- [36] D. Casellas, J. Alcala, L. Llanes, M. Anglada, Fracture variability and R-curve behavior in yttria-stabilized zirconia ceramics, Journal of materials science 36(12) (2001) 3011-3025.
- [37] J. Alcalá, M. Anglada, Fatigue and Static Crack Propagation in Yttria-Stabilized Tetragonal Zirconia Polycrystals: Crack Growth Micromechanisms and Precracking Effects, Journal of the American Ceramic Society 80(11) (1997) 2759-2772.
- [38] R.H. Dauskarat, D.B. Marshall, R.O. Ritchie, Cyclic fatigue-crack propagation in magnesia-partially-stabilized zirconia ceramics, Journal of the American Ceramic society 73(4) (1990) 893-903.
- [39] T. Liu, Y.W. Mai, G. Grathwohl, Cyclic Fatigue Crack Propagation Behavior of 9Ce-TZP Ceramics with Different Grain Size, Journal of the American Ceramic Society 76(10) (1993) 2601-2606.
- [40] A.G. Evans, R. Cannon, Toughening of brittle solids by martensitic transformations, Acta metallurgica 34(5) (1986) 761-800.
- [41] V.I. Levitas, Phase transformations, fracture, and other structural changes in inelastic materials, International Journal of Plasticity 140 (2021) 102914.
- [42] M. Asle Zaeem, N. Zhang, M. Mamivand, A review of computational modeling techniques in study and design of shape memory ceramics, Computational Materials Science 160 (2019) 120-136.
- [43] N. Zhang, M. A Asle Zaeem, Effects of grain orientations and pre-existing defects on mechanical properties and deformation mechanisms of polycrystalline yttria-stabilized tetragonal zirconia, Materialia 9 (2020) 100553.
- [44] N. Zhang, M. Asle Zaeem, Effects of twin boundaries and pre-existing defects on mechanical properties and deformation mechanisms of yttria-stabilized tetragonal zirconia, Journal of the European Ceramic Society 40(1) (2020) 108-114.
- [45] M. Mamivand, M. Asle Zaeem, H. El Kadiri, L.-Q. Chen, Phase field modeling of the tetragonal-to-monoclinic phase transformation in zirconia, Acta Materialia 61(14) (2013) 5223-5235.
- [46] M. Mamivand, M. Asle Zaeem, H. El Kadiri, Phase field modeling of stress-induced tetragonal-to-monoclinic transformation in zirconia and its effect on transformation toughening, Acta materialia 64 (2014) 208-219.
- [47] C. Cissé, M. Asle Zaeem, On the elastocaloric effect in CuAlBe shape memory alloys: A quantitative phase-field modeling approach, Computational Materials Science 183 (2020) 109808.
- [48] C. Cissé, M. Asle Zaeem, Design of NiTi-based shape memory microcomposites with enhanced elastocaloric performance by a fully thermomechanical coupled phase-field model, Materials & Design 207 (2021) 109898.
- [49] C. Cissé, M. Asle Zaeem, Transformation-induced fracture toughening in CuAlBe shape memory alloys: A phase-field study, International Journal of Mechanical Sciences 192 (2020) 106144.
- [50] C. Cissé, M. Asle Zaeem, An Asymmetric Elasto-Plastic Phase-Field Model for Shape Memory Effect, Pseudoelasticity and Thermomechanical Training in Polycrystalline Shape Memory Alloys, Acta Materialia 201 (2020) 580-595.
- [51] M. Mamivand, M. Asle Zaeem, H. El Kadiri, A review on phase field modeling of martensitic phase transformation, Computational Materials Science 77 (2013) 304-311.
- [52] O.U. Salman, A. Finel, R. Delville, D. Schryvers, The role of phase compatibility in martensite, Journal of Applied Physics 111(10) (2012) 103517.
- [53] H.K. Yeddu, T. Lookman, A. Saxena, Strain-induced martensitic transformation in stainless steels: a three-dimensional phase-field study, Acta materialia 61(18) (2013) 6972-6982.
- [54] S.M. Allen, J.W. Cahn, A microscopic theory for antiphase boundary motion and its application to antiphase domain coarsening, Acta metallurgica 27(6) (1979) 1085-1095.
- [55] N. Zhang, M. Asle Zaeem, Effects of crystal orientation and pre-existing defects on nanoscale mechanical properties of yttria-stabilized tetragonal zirconia thin films, JOM 71(11) (2019) 3869-3875.
- [56] Y. Zhang, X. Jin, T. Hsu, Thermodynamic calculation of Ms in ZrO2–CeO2–Y2O3 system, Journal of the European Ceramic Society 23(5) (2003) 685-690.
- [57] C. Wan, Y. Motohashi, T. Shibata, S. Baba, M. Ishihara, T. Hoshiya, Thermal conductivity of superplastically deformed 3Y-TZP, Materials Transactions 43(10) (2002) 2473-2479.

- [58] C. Mercer, J. Williams, D. Clarke, A. Evans, On a ferroelastic mechanism governing the toughness of metastable tetragonal-prime (t') yttria-stabilized zirconia, Proceedings of the Royal Society A: Mathematical, Physical and Engineering Sciences 463(2081) (2007) 1393-1408.
- [59] J. Cho, J. Li, H. Wang, Q. Li, Z. Fan, A. Mukherjee, W. Rheinheimer, H. Wang, X. Zhang, Study of deformation mechanisms in flash-sintered yttria-stabilized zirconia by in-situ micromechanical testing at elevated temperatures, Materials Research Letters 7(5) (2019) 194-202.
- [60] K. Knowles, D. Smith, The crystallography of the martensitic transformation in equiatomic nickel-titanium, Acta Metallurgica 29(1) (1981) 101-110.
- [61] K.F. Hane, T.W. Shield, Microstructure in the cubic to monoclinic transition in titanium–nickel shape memory alloys, Acta materialia 47(9) (1999) 2603-2617.
- [62] M. Mamivand, M. Asle Zaeem, H. El Kadiri, Effect of variant strain accommodation on the three-dimensional microstructure formation during martensitic transformation: application to zirconia, Acta Materialia 87 (2015) 45-55.
- [63] S.K. Chan, Y. Fang, M. Grimsditch, Z. Li, M.V. Nevitt, W.M. Robertson, E.S. Zouboulis, Temperature dependence of the elastic moduli of monoclinic zirconia, Journal of the American Ceramic Society 74(7) (1991) 1742-1744.
- [64] X.-S. Zhao, S.-L. Shang, Z.-K. Liu, J.-Y. Shen, Elastic properties of cubic, tetragonal and monoclinic ZrO2 from first-principles calculations, Journal of nuclear materials 415(1) (2011) 13-17.
- [65] E.H. Kisi, C.J. Howard, Elastic constants of tetragonal zirconia measured by a new powder diffraction technique, Journal of the American Ceramic Society 81(6) (1998) 1682-1684.
- [66] K.J. Bowman, I.W. Chen, Transformation textures in zirconia, Journal of the American Ceramic Society 76(1) (1993) 113-122.
- [67] S.Y. Liu, I.W. Chen, Fatigue deformation mechanisms of zirconia ceramics, Journal of the American Ceramic Society 75(5) (1992) 1191-1204.
- [68] H. Tada, P.C. Paris, G.R. Irwin, The stress analysis of cracks, Handbook, Del Research Corporation 34 (1973).
- [69] O. Vasylkiv, Y. Sakka, V.V. Skorokhod, Hardness and fracture toughness of alumina-doped tetragonal zirconia with different yttria contents, Materials Transactions 44(10) (2003) 2235-2238.
- [70] J. Pan, S.-H. Lin, Fracture mechanics and fatigue crack propagation, Fatigue Testing and Analysis (2005) 237.
- [71] H.K. Yeddu, T. Lookman, A. Saxena, The simultaneous occurrence of martensitic transformation and reversion of martensite, Materials Science and Engineering: A 594 (2014) 48-51.
- [72] A. Yamanaka, T. Takaki, Y. Tomita, Elastoplastic phase-field simulation of martensitic transformation with plastic deformation in polycrystal, International journal of mechanical sciences 52(2) (2010) 245-250.